Iron and Nickel Cellular Structures by Sintering of 3D-Printed Oxide or Metallic Particle Inks**

By *Shannon L. Taylor, Adam E. Jakus, Ramille N. Shah* and *David C. Dunand**

Inks comprised of metallic Fe or Ni powders, an elastomeric binder, and graded volatility solvents are 3D-printed via syringe extrusion and sintered to form metallic cellular structures. Similar structures are created from Fe_2O_3 and NiO particle-based inks, with an additional hydrogen reduction step before sintering. All sintered structures exhibit 92–98% relative density within their struts, with neither cracking nor visible warping despite extensive volumetric shrinkage ($\approx$70–80%) associated with reduction (for oxide powders) and sintering (for both metal and oxide powders). The cellular architectures, with overall relative densities of 32–49%, exhibit low stiffness (1–6 GPa, due to the particular architecture used), high strength (4–31 MPa), and high ductility, leading to excellent elastic and plastic energy absorption, when subjected to uniaxial compression.

1. Introduction

Cellular materials exhibit numerous advantages over dense materials due to their high specific stiffness, strength, damping, energy absorption, and surface areas.[1–4] Both iron

[*] Prof. D. C. Dunand, S. L. Taylor
Department of Materials Science and Engineering, Northwestern University, 2220 Campus Dr., Evanston, IL 60208, USA
E-mail: dunand@northwestern.edu
Dr. A. E. Jakus
Department of Materials Science and Engineering, Simpson Querrey Institute for BioNanotechnology, Northwestern University, 303 E Superior St., 11th Floor, Chicago, IL 60611, USA
Prof. R. N. Shah
Department of Materials Science and Engineering, Department of Surgery and Comprehensive Transplant Center, Department of Biomedical Engineering, Simpson Querrey Institute for BioNanotechnology, Northwestern University, 303 E Superior St., 11th Floor, Chicago, IL 60611, USA

and nickel, pure or alloyed, have potential uses in cellular architectures for energy storage,[2,5–7] emissions control,[2] catalyst supports,[1,8] and structural applications.[1,3,4,8–10] The micro-architectures of ordered, periodic cellular materials such as scaffolds, honeycombs, lattices, and trusses can be optimized to provide additional improvement on these properties over randomly oriented cellular architectures.[8,11–13] However, the widespread commercial and industrial adoption of cellular metal structures has been hindered by the fact that they are difficult and/or costly to manufacture at sufficient scales and rates relative to traditional metallic structures fabricated using long-established manufacturing methods such as casting. This is especially true for high-melting metals such as Fe and Ni which, unlike Al, are difficult to foam in the liquid state.

We recently introduced a versatile and simple process for the additive manufacturing of cellular, metallic architectures, where a liquid ink, consisting of a suspension of metal oxide or metal particles, is first 3D-printed into a structure, and this structure is then subjected to sintering, with an intermediate thermochemical reduction step if oxides are used.[14] A similar direct ink writing approach has been used to produce reticulated sheets of TiH_2 that were then rolled or folded into scrolls or origami shapes[15,16] and Ti–6Al–4V scaffolds for bone implants.[17–19] Unlike established metal additive manufacturing methods (e.g., selective laser sintering or electron-beam sintering or melting[20]), our extrusion-based method can be utilized to 3D-print complex architectures comprised of many layers from an extensive range of materials (e.g., ceramics, metals, biologics) with no required drying time and with a single 3D-printer at room temperature.[14,21] In our previous work, we 3D-printed, reduced,

and sintered metallic structures using inks comprised of either oxide or metal powders from various metallic elements (e.g., Fe, Ni, Cu, Co). [14] Oxide powders are of interest, because they are generally less expensive and less reactive (with respect to air and solvents) and thus less prone to contamination than their metal powder counterparts. However, not all oxides can be effectively reduced with hydrogen to form metals. Although we have demonstrated that either oxide or metal powders can be incorporated into 3D inks, and that both can be sintered to form metallic structures,[14] the effect of an additional reduction step (when using oxide powders) upon the properties of the final metallic structure must be further evaluated. Here, we compare the microstructure and mechanical properties of nickel and iron cellular structures 3D-printed from inks based on oxide or metallic powders.

2. Experimental Section

Oxide particle inks were synthesized through physical mixing of i) polylactic-co-glycolic acid copolymer (PLGA, 85:15 PLA-PLG by mass, from Boehringer Ingelheim, Germany); ii) Fe_2O_3 ($\geq$99%, nominal <5 μm, average particle size <1 μm) or NiO (99%, −325 mesh, average particle size 2.3 μm) powders (both from Sigma–Aldrich); and iii) a 15:2:1 by mass mixture of dichloromethane (DCM), ethylene glycol butyl ether, and dibutyl phthalate (all from Sigma–Aldrich). For every cm^3 of metal oxide powder, 16.2 g of solvent were used. The solid component of the inks is comprised of powder and PLGA in a 7:3 volume ratio. The PLGA is dissolved in approximately half of the solvent mixture in the ink cartridge (Nordson EFD 30cc fluid dispensing system). The powder is added to the remaining solvent mixture in a separate tube. After the PLGA has dissolved, the powder suspension is poured into the ink cartridge and mixed using a mini vortex mixer. Inks are then allowed to thicken at ambient temperature and pressure via DCM evaporation, with occasional hand stirring, until the viscosity reaches 30–35 Pa s. Metal inks were synthesized from Fe (99.9%, nominal 6–10 μm, average particle size 5.9 μm) and Ni (99.9%, nominal 3–7 μm, average particle size 4.4 μm) metallic powders (both from Alfa Aesar) using the same process described above for the oxide inks.

All 3D-printed structures were fabricated using a 3D-BioPlotter (EnvisionTEC, Germany) at extrusion pressures ranging from 300 to 500 kPa using a nozzle with a 510 μm inner diameter metallic tip (Nordson EFD). Cylindrical samples, 10 mm in diameter and 25 mm in height, were 3D-printed with 93 layers consisting of cylindrical struts spaced 1.2 mm apart. Each subsequent layer was rotated by 120° from the previous layer. Linear printing speeds ranged from 5 to 12 mm s^{-1}. Digital designs defining the cellular architecture were created using the EnvisionTEC custom software. The relative density of the printed objects (not including porosity within the struts) is ≈40–45%, and is determined by the fiber spacing and diameter. As-printed

samples were coated with 18 nm of osmium metal using an osmium plasma coater and then imaged using a LEO 1525 scanning electron microscope (SEM).

The particle volume fraction in the ink precursors (prior to DCM evaporation) was calculated based on the volumes, densities, and masses of all comprising components. The particle volume fraction in the 3D-printable ink (after DCM evaporation) was determined from the total ink volume and the total volume of particles within the ink. To determine the particle volume fraction in the as-printed material, $V_{f,particle}$, a 3–4 m length of continuous fiber was produced by extruding the ink through a 600 μm diameter conical tip at constant pressure, then spooled, and collected in vials. Solvents were removed from the as-printed fibers using a 2 h rinse in 70% ethanol followed by a 1 h rinse in reverse osmosis water.[21] The washed fibers were then dried overnight under vacuum at 50 °C. This washing and drying process ensured that only the PLGA and the particles remained in the fibers. The volume fraction of pores within the fibers, $V_{f,pore}$, was then determined using Equation 1:

$$V_{f,pore} = 1 - \frac{\frac{m_{fiber}}{V_{fiber}}}{0.3\rho_{PLGA} + 0.7\rho_{particle}} \qquad (1)$$

where m_{fiber} is the mass of the fiber, V_{fiber} is the volume of the fiber (calculated from the measured diameter, assuming a cylindrical fiber cross-section), ρ_{PLGA} is the density of PLGA (1.15 g cm^{-3}), and $\rho_{particle}$ is the density of the metal or oxide particles used in the ink. The volume fraction of particles is then determined from $V_{f,pore}$, and the volume fraction of PLGA ($V_{f,PLGA} = 0.3$) by mass conservation.

All 3D-printed samples were thermochemically processed in a hydrogen furnace (MTI Corporation GSL-1500X-50HG) using 99.999% pure H_2 gas (Airgas) at a flow rate of ≈160–200 mL min^{-1}. For the oxide-derived samples, the heat treatment included three separate stages: i) a pyrolysis stage of 1 h at 300 °C to remove the PLGA; ii) a reduction stage of 1 h at 600 °C to reduce the metal oxides to metal; and iii) a sintering stage of 2 h at 900 °C for the iron materials (just below the BCC to FCC transition temperature) and 4 h at 1 300 °C for the nickel materials. For the metal-derived samples, the same time-temperature profiles were used as for the oxide-derived samples but without the reduction stage. Sample dimensions and masses were measured before and after heat treatment. Metallic samples were imaged using a LEO 1525 SEM. Radial cross-sections of the metallic samples were mounted in epoxy, polished using 320, 400, 600, 800, 1 200 grit SiC grinding paper followed by 3 and 1 μm diamond suspensions and a 0.05 μm alumina suspension (all from Buehler), and imaged using a Nikon Eclipse MA200 inverted light microscope. Strut porosity was determined using ImageJ image analysis on optical images obtained from polished sample cross-sections as well as by helium pycnometry (Micrometrics AccuPyc 1330). The relative density of the metallic samples is 32–49% and was calculated from the mass and overall volume measurements.

After thermochemical processing, the top and bottom faces of the metallic samples were cut by electrical discharge machining to form cylinders with height:diameter ratios of 2:1. The cut end-pieces were used for metallography and SEM. Compression tests were performed on the metallic samples using a piston-in-sleeve compression cage with carbide inserts on an MTS Sintech 20G with an 89 kN (20 000 lb) load cell at a strain rate of $2\,mm\,min^{-1}$ until a maximum load of 15 kN was reached. Strain was measured using the crosshead displacement, corrected for machine compliance using the direct technique proposed by Kalidindi et al.[22] The yield strength was calculated as the 0.2% offset yield stress using the elastic slope.

3. Results and Discussion

3.1. Particle Packing

Figure 1 shows a schematic of the particle packing fractions throughout the 3D-printing and sintering process. In the initial ink precursors before evaporative thickening, the particles comprise only ≈5% of the total suspension volume. As the DCM evaporates and the ink thickens, the particle volume fraction increases to 15–20%, at which point the ink reaches a viscosity of 30–35 Pa s, suitable for 3D-printing.[14] As the ink is extruded from the nozzle, shear forces further compact the particles. This mechanical compaction combined with the near-instantaneous evaporation of DCM from the extruded ink and the subsequent precipitation, and corresponding volume contraction, of PLGA, results in a particle volume fraction of ∼60% (determined using Equation 1) in the struts of the as-printed structures. Figure 2a shows the typical particle packing in cross-sections of the as-printed struts for each of the four materials. This is near the maximum packing fraction for random packing of particles with uniform size, 64%;[23] however, it should be noted that the powders used in this study are not uniform in size or shape. Finally, the solid fraction increases to >90% as the polymer pyrolyzes and the particles sinter (Figure 2b). In the case of metal oxides, the reduction of the oxide also contributes to the particle sintering, as discussed later.

3.2. Mass and Dimension Changes

The relative densities of the reduced and sintered metallic cellular samples $\frac{\rho^*}{\rho_s}$, where ρ^* is the density of the cellular solid and ρ_s is the density of the solid material (7.87 g cm^{-3} for Fe and 8.91 g cm^{-3} for Ni), were calculated by dividing the mass of the sample by the total volume of the sample (measured with calipers) and comparing this to the solid density. The average relative densities for the heat-treated metallic samples are 40 ± 2% and 44 ± 5% for samples derived from Fe$_2$O$_3$ and Fe, respectively, and 41 ± 9% and 37 ± 1% for samples derived from NiO and Ni, respectively.

Although the relative densities of the oxide-derived and the metal-derived samples are similar, the overall dimensional changes and mass losses during the heat treatment are significantly different, as shown in Figure 3a. The linear shrinkage of the oxide-derived samples (44% for Fe$_2$O$_3$ and 40% for NiO) is much higher than for the metal-derived samples (20% for Fe and 29% for Ni). This is because of the additional volume change due to oxygen loss as the oxides are reduced to metals prior to sintering (≈53% from Fe$_2$O$_3$ to Fe and ≈41% from NiO to Ni, as calculated from densities and stoichiometry). An additional volume reduction of ≈30% from the removal of the PLGA binder and residual solvents
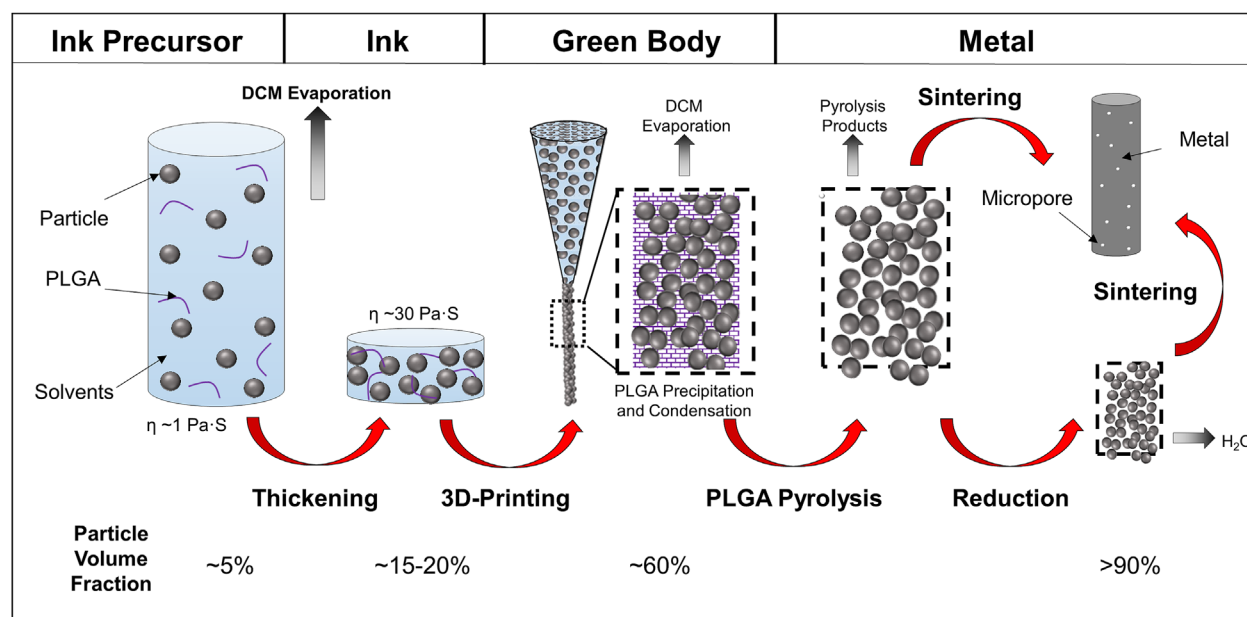

Fig. 1. Schematic of particle packing evolution during ink preparation, 3D-printing, and sintering. The volume fraction of particles in the ink precursor is initially low, but increases as the DCM evaporates and is further increased during 3D-printing as the DCM continues to evaporate and the shear forces during extrusion compact the particles. The solid fraction increases to greater than 90% as the polymer pyrolyzes, oxides are reduced, and the particles sinter.
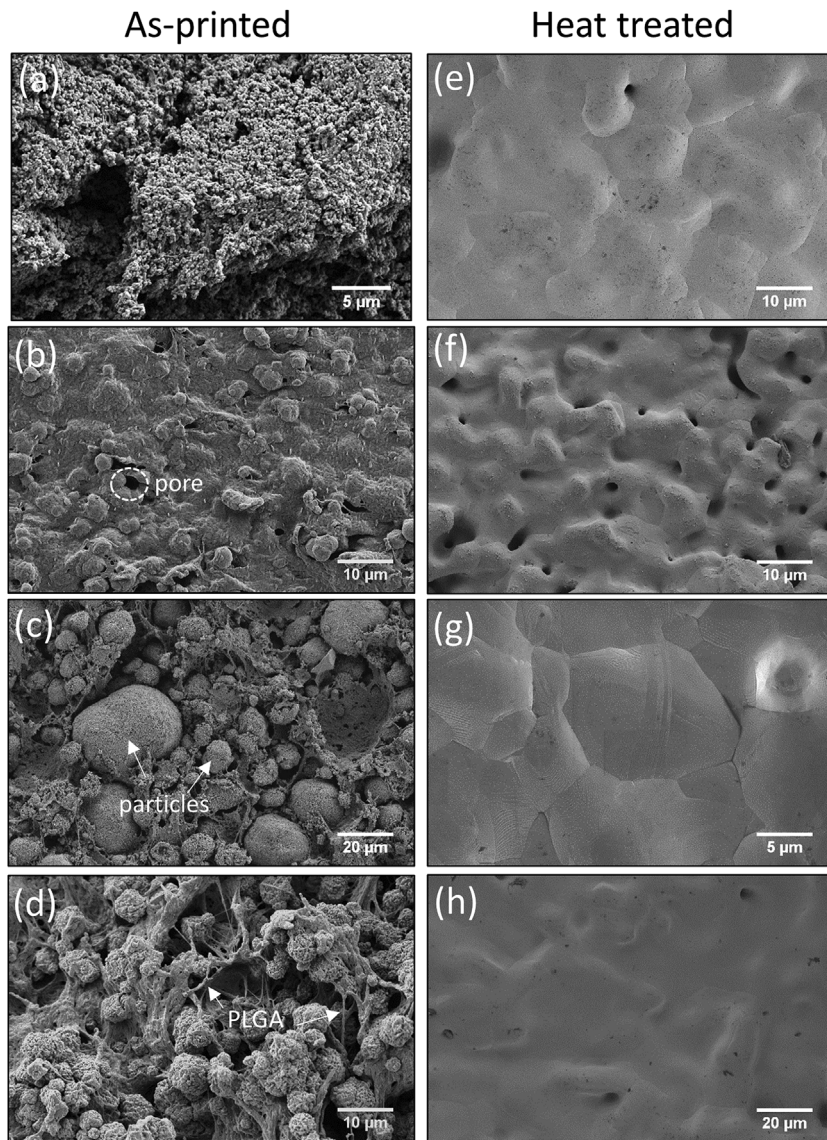
ADVANCED ENGINEERING MATERIALS

S. L. Taylor et al./Iron and Nickel Cellular Structures by Sintering...

FULL PAPER

As-printed   ## Heat treated

Fig. 2. SEM images of the surfaces of 3D-printed cellular materials before (a–d) and after (e–h) sintering in hydrogen derived from: (a, e) Fe_2O_3, (b, f) Fe, (c, g) NiO, and (d, h) Ni powder-based inks. The as-printed struts are comprised of particles, pores, and a PLGA matrix. The surfaces of the reduced and sintered struts show nearly full densification of the particles.

losses for the oxide-derived samples are two to three times larger than those for the metal-derived samples ($\approx43\%$ for Fe_2O_3 vs. $\approx12\%$ for Fe and $\approx37\%$ for NiO vs. $\approx15\%$ for Ni).

3.3. Strut Microstructure and Internal Porosity

Figure 4 shows representative optical micrographs of struts from the polished cross-sections of the iron (Figure 4a–b) and nickel (Figure 4c–d) cellular structures derived from oxide (Figure 4a,c) or metal (Figure 4b,d) powders. All structures show less than 8% internal porosity within the sintered struts and exhibit microstructures characteristic of intermediate or late-stage sintering.[23] The internal strut porosities determined by cross-sectional analysis for the iron structures derived from Fe_2O_3 and Fe are $2.0\pm0.2\%$ and $7.6\pm2.6\%$, respectively. The corresponding values for the nickel structures derived from NiO and Ni are $2.8\pm0.7\%$ and $4.0\pm2.5\%$, respectively. Pycnometry results, which measure closed porosity over the whole sample, are consistent with the porosities from the cross-sectional analysis, as expected. For both systems, the metal-derived structures have higher levels of internal porosity than, and the distribution of pores throughout the samples is not as homogeneous as, the samples derived from the respective oxides. The small, spherical pores in the oxide-derived metallic structures are characteristic of late-stage sintering whereas the larger, more tortuous pores in the metal-derived metallic objects are indicative of intermediate-stage sintering.[23] Although the nominal sizes of all metal and oxide powders were similar, the volume of the oxide powders decreases (by $\approx53\%$ for Fe_2O_3 and $\approx41\%$ for NiO as calculated from densities and stoichiometry) during reduction of the oxide to metal. The smaller size of the reduced powder enhances sintering because the sintering rate is inversely proportional to the particle size,[23] contributing to the observed differences in porosity between samples derived from the oxide versus metal particles.

The chemical reduction of oxide to metal has also been associated with an increase in the atomic diffusion rate in particles with some degree of sintering occurring prior to or during reduction because it increases the porosity, and thus decreases the diffusion distance.[24] For the samples in the present study, it is likely that some sintering occurs during the reduction step and prior to the higher temperature sintering step. Thus an increased diffusivity, coupled with a reduced particle size in the oxide-derived samples compared with the

occurs in all samples. This results in an overall measured volume shrinkage after heat treatment of $\approx82\pm2\%$ for Fe_2O_3, $\approx49\pm4\%$ for Fe, $\approx78\pm0\%$ for NiO, and $\approx64\pm2\%$ for Ni. For all materials and samples evaluated, the linear shrinkage is homogeneous and isotropic and the structures experience neither visible warping nor cracking during heat treatment (Figure 3b–i). We note that this substantial dimensional shrinkage is beneficial if it is desired to achieve printed features that are significantly finer than the tip size.

All samples lose 10–15% mass from the removal of the PLGA binder and residual solvents present within the material. Due to the loss of oxygen during reduction, the oxide-derived samples experience an additional mass loss of $\approx30\%$ for Fe_2O_3 and $\approx22\%$ for NiO (as calculated from densities and stoichiometry). Thus, the overall measured mass
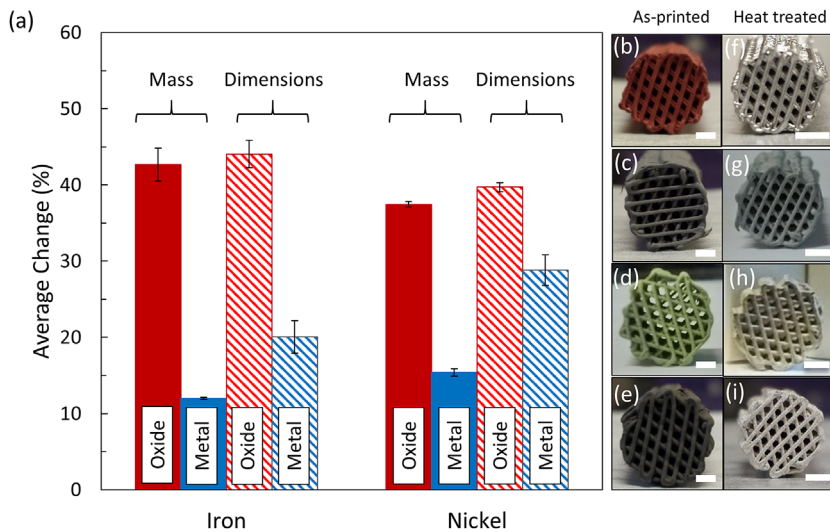
Fig. 3. (a) Graph of mass and linear dimensional changes for oxide- and metal-derived structures made of iron and nickel. Due to the loss of oxygen after oxide reduction, oxide-derived samples have greater changes in mass and dimensions than their metal-derived counterparts. Photographs of samples before (b–e) and after (f–i) heat-treatment derived from: (b, f) Fe_2O_3, (c, g) Fe, (d, h) NiO, and (e, i) Ni particle-based inks. Note the difference in scale bars, all representing 2 mm.

metal-derived samples, results in lower internal porosity. Optimization of the sintering times and temperatures could lead to even lower internal porosity.

3.4. Compressive Properties

Representative compressive stress–strain curves for each of the 3D-printed metallic cellular structures are shown in Figure 5. For all materials, the stress–strain curves illustrate the three distinct characteristic regions of metallic cellular materials and foams undergoing compression: i) a narrow elastic region at low strains (<0.2%); (ii) a wide stress plateau as plastic deformation occurs in the structure (~0.2–20%); and (iii) a sharp increase in stress during densification (>20%). The smoothness of the stress plateau (i.e., the lack of serrations) indicates that the struts of the cellular materials are plastically deforming rather than fracturing during the compression testing.[15] The gradual increase in stress within the plateau indicates strain hardening of the metals. Samples reached 60–80% strain at the maximum load without any brittle fracture, cracking, or spalling (see insets in Figure 5).

The Gibson–Ashby model for the Young's modulus of an open-cell foam, E^*, is as follows:[1]

$$\frac{E^*}{E_s} = C_1 \left(\frac{\rho^*}{\rho_s}\right)^2 \qquad (2)$$

where E_s is the Young's modulus of the bulk material (200 GPa for iron and 207 GPa for nickel)[25] and C_1 is a constant equal to unity. The relative Young's moduli of the 3D-printed cellular structures (12 samples with relative densities of 32–49%) are plotted in Figure 6a along with the predictions from the Gibson–Ashby model. The experimentally determined Young's moduli are approximately one order of magnitude lower than the predictions from Equation 2. This strong deviation from the Gibson–Ashby models for the elastic modulus of open-cell foams may be explained by the fact that, in the samples presented here, the deflection in the struts is not due to bending of horizontal struts during elastic deformation, as the model assumes. Figure 7a shows a model cross-section of the cellular architectures used in this work. During compression, the vertical load is transferred from one horizontal strut layer to the next through the strut contact areas, creating a continuous path that acts as a vertical load-bearing member. From a top-down perspective, the geometry exhibits hexagonal, honeycomb-like characteristics; however, when this architecture is loaded in compression, the vertical load-bearing
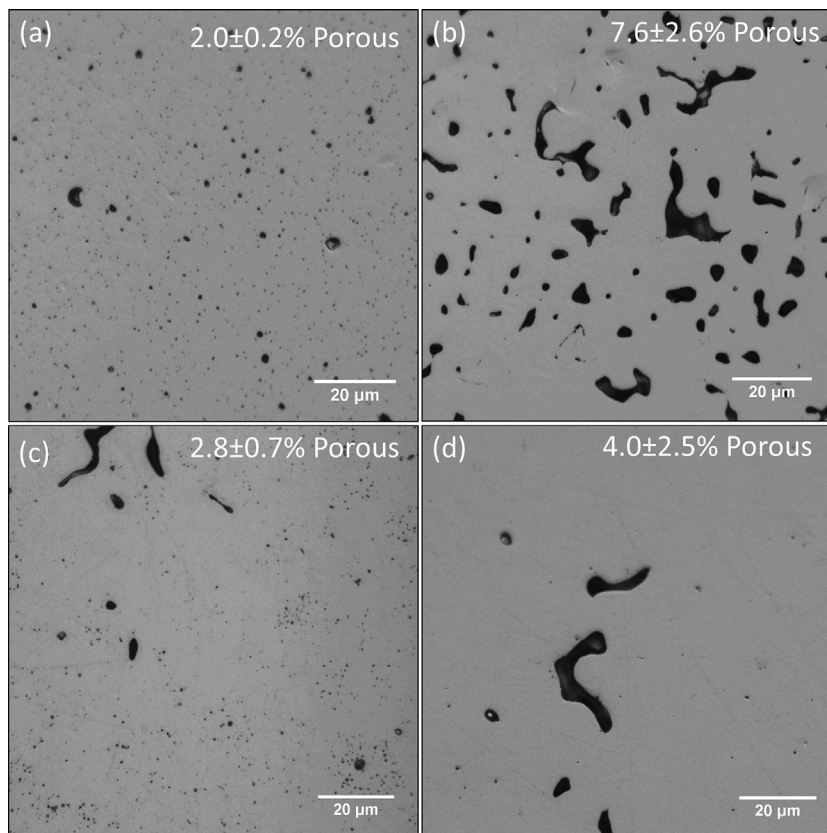

Fig. 4. Optical micrographs of polished metallographic cross-sections of struts in 3D-printed iron and nickel cellular materials after sintering derived from: (a) Fe_2O_3, (b) Fe, (c) NiO, and (d) Ni powders. Late stage sintering pores are present in (a) and (c) while (b) and (d) show residual porosity associated with intermediate stage sintering.

ADVANCED ENGINEERING MATERIALS

FULL PAPER

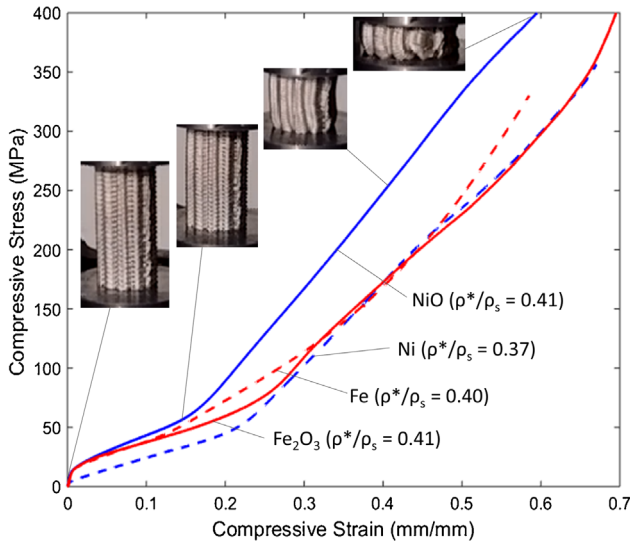S. L. Taylor et al./Iron and Nickel Cellular Structures by Sintering...

Fig. 5. Representative compressive stress–strain curves for 3D-printed iron and nickel cellular materials with similar relative densities. Each curve is labeled with the particle type from which the sample was derived and the relative density of the metal sample. The inset images show the deformation of the NiO-derived nickel sample throughout the compression testing. All of the tested samples deformed to ≈60–80% strain without any brittle fracture, cracking, or spalling.

members do not form a linear path, as in a honeycomb, but rather are reminiscent of a helical spring (outlined in white). This results in a much lower stiffness than if the horizontal layers were translated such that the load were transferred along a straight, vertical path, reminiscent of a column, as depicted in Figure 7b. A detailed analysis via finite-element modeling would shed light on the stiffness of the structure, but is beyond the scope of this paper.

The Gibson–Ashby model for the plastic yield stress of an open-cell foam with a density correction, σ_{pl}^* is as follows:[1]

$$\frac{\sigma_{pl}^*}{\sigma_s} = C_2 \left(\frac{\rho^*}{\rho_s}\right)^{3/2} \left(1 + \left(\frac{\rho^*}{\rho_s}\right)^{1/2}\right) \qquad (3)$$

where σ_s is the yield strength of the bulk material (50 MPa for iron and 59 MPa for nickel)[25] and C_2 is a constant equal to ≈0.23 for open-cell foams. The relative compressive yield strengths of the 3D-printed cellular materials along with the predictions from the Gibson–Ashby models are plotted in Figure 6b. The measured compressive yield strengths of the samples derived from Ni powders agree with the predictions from Equation 3 indicating there was little contamination from powder surface oxides or from the binder. For samples derived from Fe_2O_3, Fe, and NiO, the measured compressive yield strengths are higher than the predictions from Equation 3 by a factor of 2–4, likely as a result of residual carbon from the polymer binder diffusing into the iron and nickel during the heat treatments to provide solid solution strengthening (for iron and nickel) and precipitation strengthening (for iron);[26–28] a small volume fraction of unreduced NiO may also provide dispersion strengthening. Microhardness measurements were inconclusive, due to the small cross-section of the struts available.
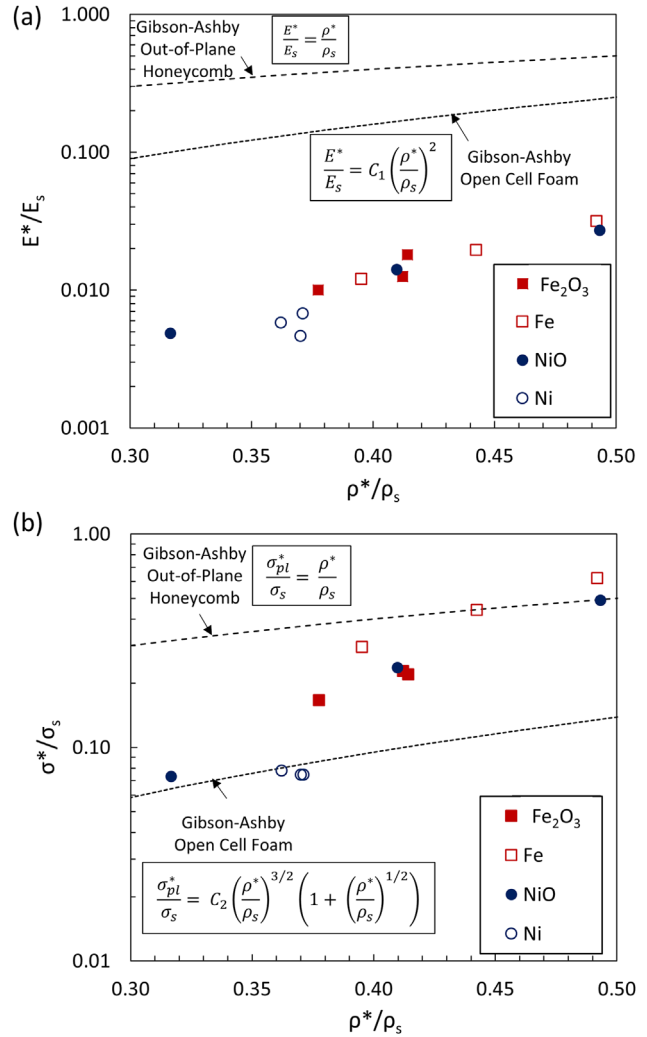

Fig. 6. Plots of (a) relative Young's modulus and (b) relative yield strength versus relative density for 3D-printed metallic cellular materials. The Gibson–Ashby models for a honeycomb loaded out-of-plane and an open cell foam are shown as dashed lines.

Increased strength from the inclusion of impurities has been reported in closed-cell ferrous foams fabricated by reduction of ceramic foam precursors.[29,30] Ti–6Al–4V porous scaffolds produced using a similar 3D-printed green body followed by a heat-treatment to remove the polymer binder and sinter the powders, were reported to have high compressive yield strengths, in some cases greater than the expected yield strength of fully dense Ti–6Al–4V.[17–19] These high yield strengths could also have been the result of oxygen or carbon contamination during heat treatment.

The compressive yield strengths of samples derived from Fe_2O_3, Fe, and NiO powders approach the predictions from the Gibson–Ashby model for the plastic yield stress of a honeycomb loaded out-of-plane, σ_{pl}^*:

$$\frac{\sigma_{pl}^*}{\sigma_s} = \frac{\rho^*}{\rho_s} \qquad (4)$$

This is consistent with the fact that the architecture of the 3D-printed objects is intermediate between a typical open-cell

S. L. Taylor et al./Iron and Nickel Cellular Structures by Sintering...

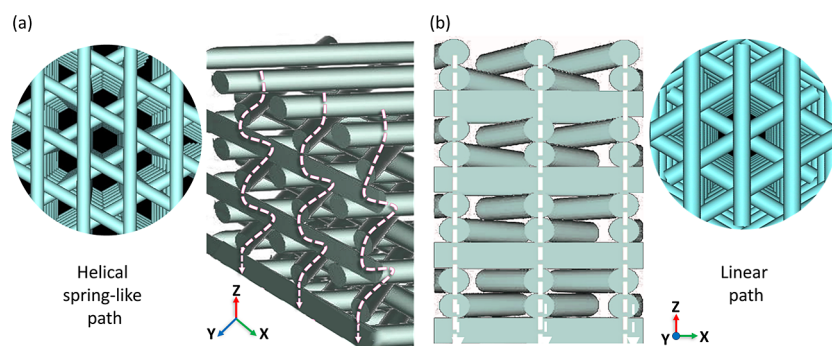**ADVANCED ENGINEERING MATERIALS**

FULL PAPER

Fig. 7. Models of radial and longitudinal cross-sections of 3D-printed metallic cellular structures with different load-bearing members (outlined in white): (a) helical spring-like path, (b) linear path. The load transfer paths due to compressive loading in the z-direction were determined by the contact areas between each layer.

foam and a typical honeycomb. It should be noted that although we compare our results to the predictions from the Gibson–Ashby models, the architectures of the 3D-printed samples are more complex than those assumed for the Gibson–Ashby models.

The stiffnesses and strengths of the 3D-printed cellular iron and nickel structures are similar to those for iron and nickel foams produced by powder metallurgy both with[29–31] and without foaming agents,[32,33] and by electroplating.[34] Over the range of relative densities studied in this work (32–49%), there are no clear differences in the elastic moduli or yield strengths of the samples derived from metal or oxide powders, indicating that the initial powders have only a minor effect on the mechanical properties, despite different levels of volume change during densification. Instead, the structural architecture (e.g., strut diameter and spacing, layer rotation and translation) dictates the mechanical behavior, because it determines both the shape and orientation of the load-bearing members and the relative density of the structure.[18] Further analysis with finite element modeling would be necessary to determine the exact mechanisms behind the elastic and plastic deformation, and to obtain the optimal combination of stiffness and strength for a given application, but is beyond the scope of this work.

The combination of low stiffness and high yield stress for the 3D-printed metallic cellular materials reported here imply that these structures can store high elastic strain energy, which is important for mechanical energy storing applications.[1] Additionally, the combination of high ductility, high yield strength, and high strain hardening of the metallic structures leads to high absorbed plastic energies (at 50% strain) ranging from 35–118 MJ m^{-3}. The upper range is nearly twice the reported upper values for the plastic strain energies of a variety of steel foams ($\approx$19–68 MJ m^{-3}) of similar relative densities.[10] Optimization of the chemical reduction and thermal sintering parameters (e.g., times, temperatures, and particle size), changes in the cellular architecture, and alloying of the pure iron and nickel cellular materials (e.g., by using prealloyed powders,[17–19] adding elemental powders directly to the inks,[14] pack cementation,[9,35,36] or carburization[37]) could further improve

the mechanical properties and expand the range of applications for these cellular materials.

4. Conclusions

We investigate here iron and nickel cellular structures (relative densities between 32 and 49%) comprised of layers of parallel struts, fabricated using a sequence of i) 3D-printing of liquid inks in which Fe_2O_3, Fe, NiO, or Ni powders are suspended; and ii) powder densification achieved by solvent evaporation, polymer pyrolysis, powder sintering, and, in the case of oxides, hydrogen reduction of the oxides to metal. The main conclusions are as follows:

1) The linear shrinkages of the oxide-derived structures (44% for Fe_2O_3, 40% for NiO) were much larger than for the metal-derived structures (20% for Fe, 29% for Ni). No visible warping or cracking was observed in any of the samples.

2) The internal porosity within the struts is lower and more homogeneously distributed for samples derived from oxide powders (2–3%) than from metal powders (4–8%), most likely because of the powder size decrease during, and the increased diffusivity associated with, the chemical reduction step.

3) The 3D-printed structures exhibit stress–strain curves typical of ductile metal cellular materials, with wide stress plateaus without serrations.

4) Their low stiffnesses (1–6 GPa) and high yield strengths (4–31 MPa) are consistent with a spring-like load-bearing member and make them suitable for applications in which a high elastic strain energy must be stored.

5) The combination of high yield stress, strain hardening, and ductility give these structures a high plastic energy absorption.

[1] L. J. Gibson, F. Ashby, Michael, *Cellular Solids: Structure and Properties*, Cambridge University Press, Cambridge, UK **1997**.

[2] V. Paserin, J. Shu, L. Renny, A. M. Liu, B. Q. Yu, M. Groo, in *MetFoam 2007 Porous Met. Met. Foam. Proc. Fifth MetFoam Conf.* (Eds: L. P. Lefebvre, J. Banhart, D. C. Dunand), DEStech Publications, Inc., Lancaster, Pennsylvania, USA **2007**, p. 121.

[3] J. Banhart, *Prog. Mater. Sci.* **2001**, *46*, 559.

[4] M. F. Ashby, R. F. M. Medalist, *Metall. Mater. Trans. A* **1983**, *14A*, 1755.

ADVANCED ENGINEERING MATERIALS

S. L. Taylor et al./Iron and Nickel Cellular Structures by Sintering...

FULL PAPER

[5] K. Otsuka, T. Kaburagi, C. Yamada, S. Takenaka, *J. Power Sources* **2003**, *122*, 111.

[6] X. Zhao, N. Xu, X. Li, Y. Gong, K. Huang, *RSC Adv.* **2012**, *2*, 10163.

[7] E. Lorente, J. A. Peña, J. Herguido, *Int. J. Hydrogen Energy* **2008**, *33*, 615.

[8] T. A. Schaedler, A. J. Jacobsen, A. Torrents, A. E. Sorensen, J. Lian, J. R. Greer, L. Valdevit, W. B. Carter, *Science* **2011**, *334*, 962.

[9] H. Choe, D. C. Dunand, *Acta Mater.* **2004**, *52*, 1283.

[10] B. H. Smith, S. Szyniszewski, J. F. Hajjar, B. W. Schafer, S. R. Arwade, *J. Construct. Steel Res.* **2012**, *71*, 1.

[11] A. G. Evans, J. W. Hutchinson, N. A. Fleck, M. F. Ashby, H. N. G. Wadley, *Prog. Mater. Sci.* **2001**, *46*, 309.

[12] L. Valdevit, A. J. Jacobsen, J. R. Greer, W. B. Carter, *J. Am. Ceram. Soc.* **2011**, *94*, 1.

[13] A. Torrents, T. A. Schaedler, A. J. Jacobsen, W. B. Carter, L. Valdevit, *Acta Mater.* **2012**, *60*, 3511.

[14] A. E. Jakus, S. L. Taylor, N. R. Geisendorfer, D. C. Dunand, R. N. Shah, *Adv. Funct. Mater.* **2015**, *25*, 6985.

[15] E. Hong, B. Y. Ahn, D. Shoji, J. A. Lewis, D. C. Dunand, *Adv. Eng. Mater.* **2011**, *13*, 1122.

[16] B. Y. Ahn, D. Shoji, C. J. Hansen, E. Hong, D. C. Dunand, J. A. Lewis, *Adv. Mater.* **2010**, *22*, 2251.

[17] J. P. Li, J. R. De Wijn, C. A. Van Blitterswijk, K. De Groot, *J. Mater. Sci. Mater. Med.* **2005**, *16*, 1159.

[18] J. P. Li, J. R. De Wijn, C. A. Van Blitterswijk, K. de Groot, *J. Biomed. Mater. Res. Part A* **2009**, *92*, 33.

[19] J. P. Li, J. R. de Wijn, C. A. Van Blitterswijk, K. de Groot, *Biomaterials* **2006**, *27*, 1223.

[20] W. E. Frazier, *J. Mater. Eng. Perform.* **2014**, *23*, 1917.

[21] A. E. Jakus, E. B. Secor, A. L. Rutz, S. W. Jordan, M. C. Hersam, *ACS Nano* **2015**, *9*, 4636.

[22] S. R. Kalidindi, A. Abusafieh, E. El-Danaf, *Exp. Mech.* **1997**, *37*, 210.

[23] R. M. German, *Powder Metallurgy Science*, Metal Powder Industries Federation, Princeton, NJ, USA **1994**.

[24] M. Kim, K. K. Kim, J. M. Smith, *AlChE J.* **1974**, *20*, 670.

[25] MatWeb, *MatWeb Material Property Data*, can be found under http://www.matweb.com/, **2015**.

[26] I. Matsui, T. Uesugi, Y. Takigawa, K. Higashi, *Acta Mater.* **2013**, *61*, 3360.

[27] ASM International, in *Pract. Heat Treat.*, ASM International, Materials Park, OH, USA **2006**.

[28] B. M. Singleton, P. Nash, *Bull. Alloy Phase Diagrams* **1989**, *10*, 121.

[29] A. Verdooren, H. M. Chan, J. L. Grenestedt, M. P. Harmer, H. S. Caram, *J. Mater. Sci.* **2005**, *40*, 4333.

[30] A. Verdooren, H. M. Chan, J. L. Grenestedt, M. P. Harmer, H. S. Caram, *J. Am. Ceram. Soc.* **2006**, *89*, 3101.

[31] L. P. Lefebvre, M. Gauthier, M. Patry, *Int. J. Powder Metall.* **2006**, *42*, 49.

[32] J. Čapek, D. Vojtěch, *Mater. Sci. Eng. C* **2014**, *43*, 494.

[33] J. Čapek, D. Vojtěch, A. Oborna, *Mater. Des.* **2015**, *83*, 468.

[34] X. Badiche, S. Forest, T. Guibert, Y. Bienvenu, J. D. Bartout, P. Ienny, M. Croset, H. Bernet, *Mater. Sci. Eng. A* **2000**, *289*, 276.

[35] D. Erdeniz, A. J. Levinson, K. W. Sharp, D. J. Rowenhorst, R. W. Fonda, D. C. Dunand, *Metall. Mater. Trans. A* **2014**, *46*, 426.

[36] D. Erdeniz, K. W. Sharp, D. C. Dunand, *Scr. Mater.* **2015**, *108*, 60.

[37] L. C. Dial, T. H. Sanders, J. K. Cochran, *Metall. Mater. Trans. A Phys. Metall. Mater. Sci.* **2012**, *43*, 1303.